Viscous Rayleigh-Taylor Instability Experiments at High Pressure and Strain Rate

Hye-Sook Park, K. T. Lorenz, R. M. Cavallo, S. M. Pollaine, S. T. Prisbrey, R. E. Rudd, R. C. Becker, J. V. Bernier, and B. A. Remington

Lawrence Livermore National Laboratory, Livermore, California 94550, USA

(Received 8 July 2009; revised manuscript received 7 December 2009; published 2 April 2010)

Experimental results showing significant reductions from classical in the Rayleigh-Taylor instability growth rate due to high pressure effective lattice viscosity are presented. Using a laser created ramped drive, vanadium samples are compressed and accelerated quasi-isentropically at ~1 Mbar peak pressures, while maintaining the sample in the solid state. Comparisons with simulations and theory indicate that the high pressure, high strain rate conditions trigger a phonon drag mechanism, resulting in the observed high effective lattice viscosity and strong stabilization of the Rayleigh-Taylor instability.

DOI: 10.1103/PhysRevLett.104.135504 PACS numbers: 62.20.F−, 62.50.−p, 68.35.Gy

When a low density fluid of density ρ_L accelerates a higher density fluid of density ρ_H, conditions for the buoyancy driven Rayleigh-Taylor (RT) instability are set up [1,2]. Perturbations at the interface can grow, generating ''bubbles'' of the lower density fluid rising into the denser fluid, and ''spikes'' of the latter sinking through the low density fluid [3]. We present experimental and simulation results that demonstrate a new RT instability stabilization mechanism at high pressure and strain rate, namely, effective lattice viscosity by phonon drag. This high pressure stabilization mechanism is predicted to increase with pressure and strain rate, provided the solid-state lattice is maintained.

A typical target in our experiment has a ''reservoir'' consisting of 40 μm thick polyimide, 125 μm thick polycarbonate, and 35 μm thick brominated polystyrene, $C_{50}H_{48}Br_2$, glued together. This is followed by a 300 μm vacuum gap, then the rippled V sample, made by sputtering V onto a mandrel that has sinusoidal ripples of $\lambda = 60$ μm wavelength and $\eta_0 = 0.6$ μm initial amplitude machined onto its surface. The back surface of the V is polished flat, and then the mandrel is chemically removed. The vanadium samples were full density, had an average grain size of ~1 μm in the lateral direction, 3–5 μm in the thickness (columnar) direction, and a measured tensile strength at ambient pressure and low-strain rate of 7.15 kbar [4]. To thermally insulate the rippled V sample from the heat created by the stagnating plasma, we use a 7–8 μm thick, CH-based epoxy ''heat shield,'' conformal on the ripple side and machined flat on the gap side. The drive calibration shots replaced the rippled V package with 10 μm Al backed by a 500 μm LiF window for interface velocity measurements.

We use six azimuthally symmetric laser beams at the Omega Laser, University of Rochester, each with $E_L \sim 135$ J energy at laser wavelength of $\lambda_L = 351$ nm and 3.7 ns square pulse shape, to generate our drive. The ~640 μm diameter flattop spatial profile is achieved using continuous phase plates on the drive beams [5], creating an average peak laser intensity of $I_L \sim 2.5 \times 10^{13}$ W/cm^2. This launches a strong shock through the reservoir which, at shock breakout, releases as a plasma across the 300 μm vacuum gap and stagnates on the V sample, creating a ~1 Mbar ramped pressure drive, as illustrated schematically in Fig. 1(a) [6,7]. Based on Newton's second law, $P \sim \rho g \Delta z$, this causes the $\Delta z = 35$ μm thick V sample to accelerate at a peak value of $g \sim 5 \times 10^{13}$ cm/s^2. The accelerating sample is RT unstable; the ripple amplitude increases at a rate that is reduced due to material strength. Density plots from 2D simulations at a sequence of times, shown in Fig. 1(b), illustrate the stabilization of RT growth due to material strength. The particle velocity (u_p) of the Al-LiF interface was measured on drive shots by a line velocity interferometer system for any reflector (VISAR) diagnostic ([8] and references therein) for a range of laser energies, as shown in Fig. 2(a). From simulations with the radiation-hydrodynamics code LASNEX [9], adjusted to reproduce this VISAR data, we generate the plasma drive: a set of material density, velocity, and temperature profiles as a function of position from the unloading reservoir just prior to impacting the sample, as illustrated in the inset of Fig. 2(a). This plasma drive applied to the V sample generates a ramped loading reaching $P_{\max} \sim 900$ kbar, as shown in Fig. 2(b), at peak compressions of $\rho/\rho_0 \sim 1.3$–1.4. The sample is predicted to stay factors of 3–5 below the calculated melt temperature based on the Lindemann law [10], as shown in the inset in Fig. 2(b).

To measure the RT ripple growth, we used face-on radiography with a 5.2 keV laser driven vanadium He-α x-ray backlighter. For area backlighting, we use a large area x-ray source and a gated x-ray camera with a 2×2 array of 15 μm pinholes configured at magnification of ~6 [11]. Alternatively, we use a ~15 μm diameter pinhole aperture placed just in front of the V backlighter foil to create a point source for projection imaging at magnification of ~19, onto a gated x-ray camera. Figure 1(c) shows example radiographs recorded at 40 ns (lower) and 80 ns (upper). The contrast (light and dark horizontal bands) are due to variations in transmitted probe x-ray intensity, $I = I_0 \exp(-z/\lambda_{\mathrm{mfp}})$, where I_0 is the incident probe x-ray

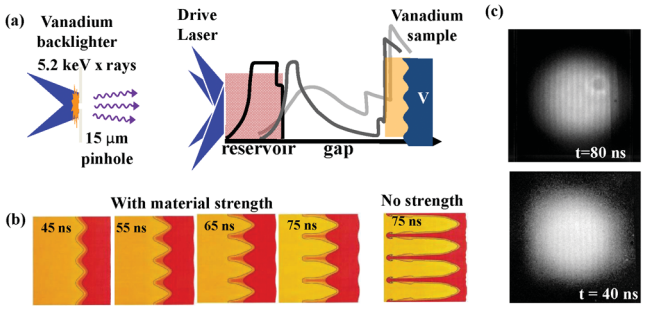

FIG. 1 (color). (a) Schematic illustrating the experimental configuration. (b) Density plots of the RT growth from 2D radiation-hydrodynamics simulations at 45, 55, 65, and 75 ns, using the PTW strength model. The second plot at 75 ns (far right-hand side) is for a simulation where V has no strength, showing the much greater RT growth. (c) Experimental x-ray radiographs of driven vanadium RT samples at 40 and 80 ns.

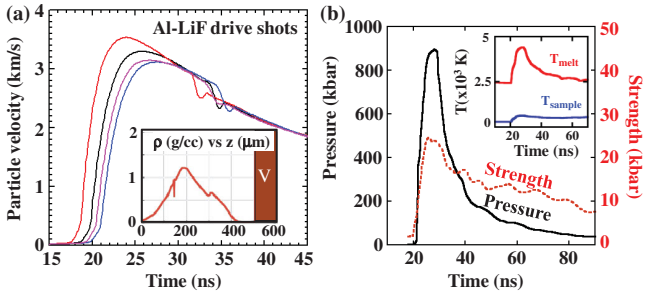

FIG. 2 (color). Drive characterization. (a) Line VISAR measurements of particle velocity at the Al-LiF interface for a 10 μm Al foil backed by a ~500 μm thick LiF window at four different laser energies, $E_L = 743$, 776, 790, and 818 J. The inset shows the result of a simulation giving density versus position, $\rho(z)$, of the shock-released reservoir "plasma drive." b) Corresponding pressure versus time in the vanadium sample (solid black curve), as calculated from the radiation-hydrodynamics simulations. The dotted red curve gives the strength versus time predicted from the simulation using the PTW strength model with input parameters modified to reproduce the RT experiment. The inset shows the Lindemann law melt temperature (red curve) and sample temperature (blue curve) from the simulations.

intensity, I is the transmitted intensity, λ_{mfp} is the x-ray mean free path length, and z is the vanadium foil thickness. The RT growth causes foil thickness modulations of increasing depth, Δz, which cause x-ray optical depth modulations, $\Delta\mathrm{OD} = \Delta z/\lambda_{\mathrm{mfp}}$. The lineouts of radiographic images of the ripples, averaged over a 120 μm vertical window at the center of each image, were fitted using $\ln(I_\nu/I) = a\sin(\frac{2\pi}{\lambda} - \varphi)$. Here I is the average probe x-ray intensity through the rippled foil, I_ν is the intensity in the ripple valleys (thinner regions of the foil, so brighter regions of transmitted probe x rays), and a, λ, and φ are the fitted amplitude, wavelength, and the phase of the ripple. The perturbation growth is written as a growth factor, $\mathrm{GF}(t) = \Delta\mathrm{OD}(t)/(\Delta\mathrm{OD}_0 \times \mathrm{MTF})$, where $\Delta\mathrm{OD}(t)$ is the modulation in optical depth at time t due to the ripple, $\Delta\mathrm{OD}_0 = \eta_0/\lambda_{\mathrm{mfp}}$ is the initial optical depth, where η_0 is the initial rippled amplitude, $\lambda_{\mathrm{mfp}} \sim 19.6$ μm is the mean free path length of the 5.2 keV backlighter x rays in vanadium, and MTF is the modulation transfer function. The $\Delta\mathrm{OD}(t)$ is determined from the radiograph by a Fourier analysis of the ripple lineouts. The MTF, which quantifies the diagnostic spatial resolution, is measured on separate shots using a resolution grid: MTF > 0.8 for the $\lambda = 60$ μm ripples used in this experiment.

We compare our RT growth factor measurements to the results from 2D radiation-hydrodynamics simulations including a constitutive strength model. The Preston-Tonks-Wallace (PTW) strength model is strain rate dependent, and is based on the deformation mechanisms of thermal activation for low-strain rates and viscous phonon drag for high-strain rates [12]. The PTW strength in the low-strain limit is expressed as

$$\sigma_y \approx 2G\max\{y_0 - (y_0 - y_\infty)\mathrm{erf}[k\hat{T}\ln(\gamma\dot{\xi}/\dot{\varepsilon})], s_0(\dot{\varepsilon}/\gamma\dot{\xi})^\beta\},$$

where $G = G(P, T)$ is the pressure dependent shear modulus, erf is the mathematical error function [13], $\dot{\varepsilon}$ is the strain rate, $\hat{T} = T/T_{\mathrm{melt}}$ is the normalized temperature, $T_{\mathrm{melt}}(\rho)$ is the Lindeman law melt temperature [10], $\dot{\xi}$ is a reference inverse time scale, $\gamma\dot{\xi} = \dot{\varepsilon}_{\mathrm{crit}}$ is the critical strain rate above which the deformation switches from thermal activation to phonon drag, and y_0, y_∞, κ, γ, s_0, and β are material dependent input parameters. These parameters roughly correspond to material properties according to $\gamma \sim \rho_{\mathrm{disloc}}b^2$, $\kappa \sim 1/U_k$, $y_\infty \sim \sigma_A$, $y_0 \sim \sigma_A + \sigma_P$, and $y_0 - y_\infty \sim \sigma_P$, where ρ_{disloc}, b, U_k, σ_A, and σ_P represent dislocation density, Burgers vector, kink activation energy, athermal strength component, and Peierls stress, respectively [14]. The PTW strength σ_s in the high-strain (saturated) limit has a similar form, only with s_0 and s_∞ replacing y_0 and y_∞. These two limits are interpolated in between by a Voce work hardening prescription for arbitrary strain ε [12].

After normalizing to the laser energy of 820 J, the self-consistent data set of GF(t) spanning several shot campaigns is shown by the red square symbols in Fig. 3. Typical experimental errors are estimated to be $\delta\mathrm{GF}/\mathrm{GF} \sim 10\%$. We estimate an average strain rate, $\dot{\varepsilon}_{\mathrm{av}} \sim 3 \times 10^7$ s^{-1}, by fitting a linear slope to the calculated strain over the interval of 25–40 ns. For $t > 40$ ns, this drops to $\dot{\varepsilon}_{\mathrm{av}} \sim 3 \times 10^6$ s^{-1}. The top curve ("no strength") corresponds to a 2D simulation of the RT growth with material strength turned off, and overpredicts the experimental data at 70 ns by a factor of ~6. A simulation using the PTW model with the default input parameters [12] is shown by the next highest curve ("PTW_nominal"), and also considerably overpredicts the experimental data. To fit our data with the PTW model in Fig. 3 (solid blue curve, "PTW_mod"), we lowered the critical strain rate for the transition from the thermal activation to the phonon drag

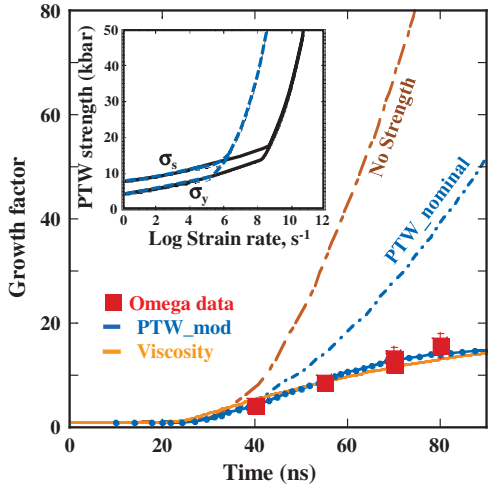

FIG. 3 (color). Measured and simulated Rayleigh-Taylor (RT) growth factors (ripple amplitude divided by initial amplitude) versus time. The solid red square plotting symbols give the experimental data. The top curve (dot-dashed brown) gives the result from the 2D simulation with strength set to zero. The dot-dashed blue curve gives the result using the PTW strength model, with default input parameters for vanadium. The solid blue curve corresponds to the PTW model, with the default vanadium input parameters γ, y_0, s_0 multiplied by 1/800, 0.60, and 0.68, respectively. The solid orange curve corresponds to an analytic approach treating the material strength as an effective lattice viscosity, with a constant value of viscosity of 400 P. The inset gives the PTW strength versus $\log(\dot{\varepsilon})$ for the low-strain limit (σ_y) and the saturated, high-strain limit (σ_s) for default (black solid) and for the modified (blue dashed) input parameters, assuming pressure $P = 500$ kbar, temperature $T = 500$ K, and compression $\rho/\rho_0 = 1.236$.

regime from the default value of $\gamma\dot{\xi} \sim 10^9$ to $\sim 10^6$ s^{-1}, accomplished by multiplying the PTW input parameters γ, y_0, and s_0 by 1/800, 0.60, and 0.68, respectively. The default PTW parameters for V in the high-$\dot{\varepsilon}$ regime were set by comparisons with overdriven shock experiments in Ta, also a bcc metal, at $d\varepsilon/dt > 10^9$ s^{-1} [12]. Furthermore, the strain rate interval of 10^4–10^9 s^{-1} was not modeled but rather "filled in" with PTW, due to the absence of reliable data to fit. So, it is not surprising that substantial changes in these input parameters for ramp loaded V were required. These changes to the PTW input parameters leave the strength predictions at $\dot{\varepsilon} < 10^6$ s^{-1} (thermal activation regime) largely unchanged [15], while increasing the strength for $\dot{\varepsilon} > 10^6$ s^{-1} (phonon drag regime), as shown in the inset of Fig. 3. It is interesting to note that the Steinberg-Lund strength model [16], which has several features similar to the PTW model, predicts the transition from thermal activation to phonon drag in vanadium would occur at $\dot{\varepsilon}_{\rm crit} \sim 10^5$ s^{-1} for default input parameters. Hence, the critical strain rate for the transition from thermal activation to phonon drag is uncertain by factors of 10^3–10^4, due to the lack of data in this high-$\dot{\varepsilon}$ regime. The dotted red curve in Fig. 2(b) shows the spatially averaged V strength versus time for the PTW model, after averaging over ~ns level temporal fluctuations; the maximum strength occurs at the time of peak pressure and strain rate. The calculated peak strength for our RT experiments, $\sigma_{\rm max} \sim 25$ kbar, corresponds to a peak pressure and strain rate of 900 kbar and 3×10^7 s^{-1}. This is a factor of 3.5 higher than the measured ambient strength of 7.15 kbar [4]. Recent theoretical work shows that the shear modulus is not expected to increase significantly with pressure in this pressure range [17]. This suggests that our observed strength increase is due to strain rate effects rather than pressure. We estimate an overall ~20% uncertainty in our $\sigma_{\rm max} \sim 25$ kbar peak strength result, based on 10% due to the uncertainties in the growth factor measurements, 10% due to the uncertainties in our plasma drive, and 10% due to potential model dependence in our analysis, all added in quadrature.

We now compare to an analytic RT growth model that treats strength as an effective lattice viscosity. In the linear regime, classical RT growth can be written as $\mathrm{GF} \approx e^{\int \gamma_{\rm classical} dt}$, where $\gamma_{\rm classical} \approx [A\frac{2\pi}{\lambda} g(t)]^{1/2}$ gives the growth rate for inviscid fluids, and A, λ, and g are the Atwood number, perturbation wavelength, and foil acceleration, respectively. For viscous fluids, the RT growth rate is determined from $\gamma_{\rm RT}^2 + 2k^2\nu\gamma_{\rm RT} - gkA = 0$ [18,19], where $\nu(\mathrm{cm}^2/\mathrm{s}) = \mu/\rho$ is the kinematic viscosity, $\mu(\mathrm{dyn\,s/cm}^2 = \mathrm{P})$ is the dynamic viscosity, and ρ is density. We show these analytic results for RT growth factors versus perturbation wavelength at 70 ns in Fig. 4. Experimental data were taken at $\lambda = 40$ and 60 μm (red squares). The 2D simulations were done at $\lambda = 40$, 60, and 100 μm with the modified PTW strength model (blue diamonds). The smooth curves in Fig. 4 correspond to (in order from the top) dynamic viscosities of 0, 100, 200, 400, and 800 P, with a best fit using $\mu \sim 400$ P. We show also in Fig. 3 the growth factor time evolution for the viscous model using 400 P. As a consistency check, we use a relationship equating strength σ with an effective lattice viscosity, $\nu = \mu/\rho \approx \sigma/(\sqrt{6}\rho\langle\dot{\varepsilon}\rangle)$ [19], giving $\sigma \approx \sqrt{6}\langle\dot{\varepsilon}\rangle\mu$. Using an average strain rate of $\langle\dot{\varepsilon}\rangle \approx 3 \times 10^7$ s^{-1} over the interval of 25–40 ns from the 1D radiation-hydrodynamics simulations and the fitted viscosity of 400 P gives an estimated peak strength of $\sigma_{\rm max} \sim 29$ kbar. For a second estimate, we make a rough approximation of strain rate from $\langle\dot{\varepsilon}\rangle \approx \frac{1}{3}\dot{\rho}/\rho \approx \frac{1}{3}(\Delta\rho/\rho_0)/\Delta t_{\rm rise\ time}$ [6]. The equation of state of V [20] allows an estimate of compression at $\rho/\rho_0 \sim 1.4$, which occurs over the measured rise time of ~6 ns, giving $\langle\dot{\varepsilon}\rangle \approx 2 \times 10^7$ s^{-1}. This gives a second estimate of peak strength of $\sigma_{\rm max} \sim 19$ kbar. These two analytic approximations bracket to within ~20% the more accurate result for the strength at peak pressure of $\sigma_{\rm max} \sim 25$ kbar inferred from the 2D RT simulations, shown in Fig. 2(b).

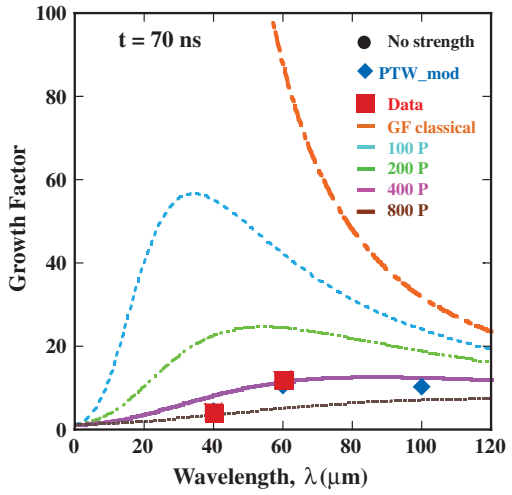

FIG. 4 (color). Measured, simulated, and analytic RT dispersion curves, given as growth factor versus perturbation wavelength at a time of 70 ns. The blue diamond solid plotting symbols correspond to a simulation with the PTW strength model adjusted to fit the experiment. The square red plotting symbols at $\lambda = 40$ and 60 μm correspond to the experimental measurements. The smooth curves correspond to the analytic viscous RT model assuming viscosities of (from the top) 0, 100, 200, 400, and 800 P.

We now relate our inferred macroscopic fluid viscosity of ~400 P to the microscopic dislocation drag coefficient in the phonon drag regime of high-strain rate deformation. A macroscopic viscosity for our experiment can be defined by $\sigma_{\text{shear}} \sim \mu v_{\text{RT}}/\lambda_{\text{RT}}$, where μ is the dynamic viscosity, σ_{shear} is the shear stress causing the RT growth, and v_{RT} is the RT bubble velocity for perturbation of wavelength λ_{RT}. At the lattice level, applied shear stress is related to dislocation velocity by $\sigma_{\text{shear}} b = MBv_{\text{disloc}}$, where $M \sim 2.75$ is the Taylor factor (to account for the glide plane orientation), b is the Burgers vector, and B is the dislocation drag coefficient [21]. And Orowan's equation relates macroscopic strain rate to microscopic parameters, $\dot{\varepsilon} = \rho_{\text{disloc}} b v_{\text{disloc}}/M$, where ρ_{disloc} is the dislocation density. These three equations can be combined to give $\mu/B \sim M^2/(\rho_{\text{disloc}} b^2)$. Taking a dislocation density of $\sim 10^{11}$ cm^{-2} from a multiscale simulation of our RT experiment [22], and assuming $b \sim 2.5$ Å under compression, gives $\mu/B \sim 4 \times 10^4$. We conclude that our inferred effective lattice viscosity of ~400 P corresponds to an order of magnitude estimate of the dislocation drag coefficient of ~0.01 dyn s/cm^2 in the phonon drag regime under the peak pressure (~1 Mbar) and strain rate ($\sim 10^7$ s^{-1}) conditions of our vanadium RT experiment. Interestingly, Nemat-Nasser and Guo infer a similar value for the drag coefficient of V and Ta, $B \sim 10^{-3}$ Pa s = 10^{-2} dyn s/cm^2, in their Hopkinson bar experiments at strain rates of 2500–8000 s^{-1} and dislocation densities of $\sim 10^9$ cm^{-2} [23].

This work was performed under the auspices of the Lawrence Livermore National Security, LLC, (LLNS) under Contract No. DE-AC52-07NA27344.

[1] Lord Rayleigh, Philos. Mag. **34**, 145 (1892).
[2] G. Taylor, Proc. R. Soc. A **201**, 192 (1950).
[3] D. H. Sharp, Physica (Amsterdam) **12D**, 3 (1984).
[4] A. F. Jankowski, J. Go, and J. P. Hayes, Surf. Coat. Technol. **202**, 957 (2007).
[5] C. A. Haynam *et al.*, Appl. Opt. **46**, 3276 (2007).
[6] J. Edwards *et al.*, Phys. Rev. Lett. **92**, 075002 (2004).
[7] K. T. Lorenz *et al.*, High Energy Density Phys. **2**, 113 (2006).
[8] R. Barker and J. Hollenbach, Appl. Phys. **43**, 4669 (1972); P. M. Celliers *et al.*, Rev. Sci. Instrum. **75**, 4916 (2004); P. M. Celliers *et al.*, Appl. Phys. Lett. **73**, 1320 (1998).
[9] G. B. Zimmerman and W. L. Kruer, Comments Plasma Phys. Controlled Fusion **2**, 51 (1975).
[10] David A. Young, *Phase Diagrams of the Elements* (University of California Pres, Berkeley, 1991); D. J. Steinberg, S. G. Cochran, and M. W. Guinan, J. Appl. Phys. **51**, 1498 (1980).
[11] K. T. Lorenz *et al.*, Phys. Plasmas **12**, 056309 (2005).
[12] D. L. Preston, D. L. Tonks, and D. C. Wallace, J. Appl. Phys. **93**, 211 (2003).
[13] M. Abramowitz and I. A. Stegum, *Handbook of Mathematical Functions* (Dover, Mineola, NY, 1965).
[14] B. A. Remington *et al.*, in *Proceedings of the Conference of the American Physical Society Topical Group on Shock Compression of Condensed Matter, Baltimore, 2005*, edited by M. D. Furnish, M. Elert, T. P. Russell, and C. T. White (AIP, New York, 2006), p. 765.
[15] B. A. Remington *et al.*, Mater. Sci. Technol. **22**, 474 (2006).
[16] D. J. Steinberg and C. M. Lund, J. Appl. Phys. **65**, 1528 (1989).
[17] R. E. Rudd and J. E. Klepeis, J. Appl. Phys. **104**, 093528 (2008).
[18] K. O. Mikaelian, Phys. Rev. E **47**, 375 (1993).
[19] J. D. Colvin *et al.*, J. Appl. Phys. **93**, 5287 (2003).
[20] *High-Velocity Impact Phenomena*, edited by Ray Kinslow (Academic, New York, 1970), p. 538.
[21] M. A. Meyers and K. K. Chawla, *Mechanical Metallurgy: Principles and Applications* (Prentice-Hall, Englewood Cliffs, NJ, 1984).
[22] R. Becker *et al.*, LLNL Internal Report No. LLNL-TR-416095, 2009.
[23] Sia Nemat-Nasser and Weiguo Guo, Mech. Mater. **32**, 243 (2000).